Research Square

Preprints are preliminary reports that have not undergone peer review.
They should not be considered conclusive, used to inform clinical practice,
or referenced by the media as validated information.

Toward Spatially Sharper Precipitation Prediction via Global-Local Frequency Guidance

Subin An
Seoul National University
Youngwook Kim
Seoul National University
Dongjin Cho
Seoul National University
Yoo-Geun Ham
yoogeun@snu.ac.kr
Seoul National University

Article

Keywords: Precipitation Prediction, Deep Learning, High-Frequency Preservation, Composite Loss Function, Wavelet-Fourier Composite Loss (WFCL)

Posted Date: March 26th, 2026

DOI: https://doi.org/10.21203/rs.3.rs-9166093/v1

License: This work is licensed under a Creative Commons Attribution 4.0 International License.
Read Full License

Additional Declarations: No competing interests reported.

Version of Record: A version of this preprint was published at npj Climate and Atmospheric Science on June 22nd, 2026. See the published version at https://doi.org/10.1038/s41612-026-01472-y.

Toward Spatially Sharper Precipitation Prediction via Global-Local Frequency Guidance

Subin An[1], Youngwook Kim[2], Dongjin Cho[3]* and Yoo-Geun Ham[1,3]*

[1]Department of Environmental Managements, Graduate School of Environmental Studies, Seoul National University, Seoul, Republic of Korea

[2]School of Earth and Environmental Sciences, Seoul National University, Seoul, Republic of Korea

[3]Environmental Planning Institute, Seoul National University, Seoul, Republic of Korea

Correspondence to: Dongjin Cho (djcho1582@snu.ac.kr), Yoo-Geun Ham (yoogeun@snu.ac.kr)

Abstract

Precipitation prediction is critical for water-related hazard preparedness, and deep learning has shown strong potential. However, conventional mean squared error (MSE) training oversmooths high-frequency variability, producing blurred precipitation fields. Although frequency-domain losses such as Fourier Amplitude and Correlation Loss (FACL) enhance global spectral consistency, they lack constraints on local phase coherence. To address this, we develop the Wavelet-Fourier Composite Loss (WFCL), integrating Wavelet Amplitude and Correlation Loss (WACL) based on the Dual-Tree Complex Wavelet Transform with FACL to jointly enforce global spectral alignment and localized phase coherence. Experiments with a U-Net show WFCL consistently outperforms MSE and FACL, maintaining stable performance across 1–3 day lead times (2018–2023). It reduces lead-time-averaged Learned Perceptual Image Patch Similarity from 0.1980 to 0.1067 relative to MSE and improves Local Phase Coherence by about 21%. In addition, for 1-day prediction, WFCL reduces Regional Histogram Distance by approximately 24% locally and 52% globally compared with FACL.

Keywords: Precipitation Prediction, Deep Learning, High-Frequency Preservation, Composite Loss Function, Wavelet-Fourier Composite Loss (WFCL)

Introduction

Precipitation is a key variable in climate and hydrological systems, influencing floods, landslides, and water availability across agricultural and urban environments (Chen & Wang, 2022; Abbas et al., 2022; Marengo et al., 2020; Hrour et al., 2020). Recent climate change has intensified both the frequency and magnitude of precipitation, particularly over mid- and high-latitude regions, driven by enhanced moisture transport, prolonged weather systems, and the increased moisture-holding capacity of a warmer atmosphere (IPCC, 2021; Trenberth, 2011; Ham et al., 2023). Global analyses for the period 1891-2019 indicate statistically significant precipitation increases across approximately 32% of regions, consistent with recent extreme events such as the 2021 European floods and the heavy rainfall associated with Typhoon Yagi in 2024 (Staal & Koren, 2023; Mohr et al., 2022; Nazeri Tahroudi, 2025; Leelawat et al., 2025). Therefore, the increasing intensity and variability of precipitation highlight the need for accurate regional precipitation prediction to support disaster risk management and climate adaptation.

Numerical weather prediction (NWP) models have been widely used for operational precipitation forecasting, but challenges remain in accurately representing precipitation at regional and convective scales (Vasić et al., 2007; Pedder et al., 2000; Bannister et al., 2020). These challenges arise from the uncertainties in physical parameterizations, including cloud microphysics and topographic gravity waves, which constrain forecast skill across multiple spatial scales (Yano et al., 2018; Lee et al., 2018; Liu et al., 2024). In recent years, data-driven deep learning models have rapidly advanced as an alternative approach to address these challenges, as they can effectively capture the complex spatiotemporal structures of precipitation through learning from large-scale observational data, offering both high computational efficiency and improved predictive accuracy (Purohit et al., 2024; Muhammad & Kareem, 2025; Yen et al., 2019; Sadeghi et al., 2019). Early studies on precipitation forecasting using deep learning approaches (e.g., convolutional long short-term memory (ConvLSTM) and generative adversarial network (GAN)-based models) demonstrated competitive skill relative to NWP models at short to medium lead times (Shi et al., 2015; Li et al., 2024; Chen et al., 2022; Wang et al., 2023).

However, deep learning models have suffered similar problem in NWP models; it has shown promising performance at large scales, while representing sub-synoptic and mesoscale

precipitation features remains challenging (Duncan et al., 2022). It is associated with the training strategy that many existing studies rely on pixel-wise loss functions such as mean squared error (MSE), which penalize both intensity and spatial displacement errors. As a result, spatially realistic but slightly displaced forecasts are penalized twice, suffering the so-called double-penalty problem (Subich et al., 2025; Zhao et al., 2024; Guilloteau et al., 2023). This indicates that the training objectives dominated by MSE discourage the representation of small-scale and high-frequency variability, leading to spatially smoothed predictions and systematic underestimation of localized convective extremes (Cao et al., 2025; Muller & Yukari, 2020). From a spectral perspective, this manifests as reduced spectral amplitude when phase alignment is imperfect, ultimately weakening sharp rainfall gradients and localized extreme precipitation signals (Dunstan et al., 2025; Subich et al., 2025). In practical forecasting, predictions that preserve the intensity and structural organization of extreme precipitation even with slight spatial tolerance are often more valuable than weak and smoothed but perfectly aligned forecasts. This perspective aligns with recent deep learning-based nowcasting studies that prioritize intensity realism and spatial coherence over strict pixel-level accuracy (Ravuri et al., 2021), indicating that modest tolerance in spatial coherence errors can be accommodated when intensity and spatial coherence are treated as distinct structural attributes.

To address these limitations, the Fourier Amplitude and Correlation Loss (FACL) was introduced to decouple amplitude and phase information that are entangled in conventional MSE-based losses. Specifically, the Fourier Amplitude Loss (FAL) regularizes the Fourier amplitude spectrum to constrain spectral energy distribution, while the Fourier Correlation Loss (FCL) enforces phase alignment between predictions and observations (Yan et al., 2024). However, because FACL operates on global frequency representation with limited capacity to capture local phase coherence, hindering a balanced treatment of global and local structures (Shi et al., 2025; Wirsing, 2020). Local phase coherence plays a critical role in preserving sharp spatial structures. Sharp boundaries and localized features exhibit consistent phase alignment across scales, whereas blurring induces scale-dependent phase shifts that weaken structural clarity (Wang & Simoncelli, 2003; Tao & Orchard, 2000). Since perceptual sharpness fundamentally depends on phase alignment, phase inconsistencies across different spatial scales in the observed field can disrupt this alignment. The human visual system is particularly sensitive to such cross-scale phase discrepancies and tends to interpret them as blur. (Wang &

Simoncelli, 2003; Caelli & Bevan, 1982). Consequently, explicitly accounting for local phase alignment is necessary to mitigate blurring and enhance spatial sharpness.

Given the limitations of global frequency-based loss and the importance of local phase coherence, this study aims to develop a composite loss framework that jointly captures global and local phase characteristics for improved precipitation prediction. To this end, we introduce the Dual-Tree Complex Wavelet Transform (DTCWT) to extract multi-scale, directionally localized amplitude and phase representations, from which a wavelet-domain amplitude-phase term is constructed (Kingsbury, 1998; Abbas & Tran, 2008). This term is then additively combined with the global FACL term to form the final loss function named as the Wavelet-Fourier Composite Loss (WFCL). To evaluate the effect of the proposed loss, we conduct precipitation prediction experiments within an identical U-Net architecture with FACL, or WFCL losses, systematically comparing its performance with the baseline (i.e., MSE) loss function. Performance is assessed using perceptual and structural metrics, along with extreme precipitation case studies, with particular emphasis on spatial sharpness and phase coherence.

Results

Evaluation of 1-day lead prediction skill and spatial-frequency analysis

In the comparative evaluation at a 1-day lead time, FACL outperforms the baseline MSE model in terms of structural quality and spatial forecasting skill, indicating improved representation of coherent precipitation patterns (Table 1). However, this advantage comes at the expense of extreme event detection, as FACL underperforms MSE in the CSI-R95p metric. In contrast, WFCL delivers consistent improvements across both structural fidelity and extreme precipitation detection. WFCL increases CSI-R95p from the MSE baseline value of 0.1446 to 0.1448, thereby overcoming the extreme-event weakness observed in FACL. At the same time, WFCL outperforms FACL across all other major metrics. Specifically, LPIPS is reduced from 0.1980 to 0.1067 (about 46%), and RHD decreases from 2.99 to 1.05 (about 65%), indicating substantial improvements in perceptual quality and spatial localization accuracy. Furthermore, FSS increases from 0.7437 to 0.8801, confirming enhanced spatial coherence. Collectively, these results demonstrate that WFCL not only refines structural representation but also significantly strengthens both localization accuracy and perceptual fidelity. To further examine the influence of decomposition depth on model performance, additional experiments were

conducted across different DTCWT levels (Level 1-3), and the results are summarized in Table S1.

Figure 1 further illustrates how these structure-preserving behaviors appear in perceptual representations, presenting global LPIPS maps and corresponding difference maps at a 1-day lead time. FACL provides overall improvements relative to MSE (Figure 1a); however, relatively high LPIPS values persist in regions dominated by strongly organized tropical precipitation, particularly over the equatorial Pacific and the western Pacific warm pool, where deep convection and pronounced rainband structures are prevalent (Chen & Houze, 1997; Houze et al., 2000). These regions appear especially sensitive to phase alignment and spatial coherence, indicating that preserving global precipitation features such as its amplitude and phase solely based on the Fourier Transform does not fully resolve perceptual discrepancies in localized precipitation structures. In contrast, WFCL yields further improvements over tropical regions and parts of the Atlantic, where precipitation is frequently governed by large-scale convective systems and linear or banded rainfall structures. The LPIPS difference maps further highlight these improvements of the WFCL-based model (Figure 1b); WFCL exhibits coherent and positive LPIPS reductions relative to MSE and FACL across most regions, with especially pronounced improvements over the tropical belt and adjacent oceanic areas. These patterns underscore the added value of incorporating local phase coherence alongside global spectral constraints for more faithful reconstruction of precipitation morphology.

Table 1. Comparison of the quantitative performance of models trained with different loss functions at a 1-day lead time. The best score for each metric is highlighted in bold, and arrows denote whether higher (↑) or lower (↓) values indicate better performance. LPC values are multiplied by 10^4 for readability, as the original LPC magnitudes are on the order of 10^{-4}.

Loss	Perceptual / Structural			Localization	Extreme Events	Spatial Skill
	LPIPS↓	CPBD↑	LPC(x10^4)↓	RHD↓	CSI-R95p↑	FSS↑
MSE	0.1980	85.85	2.82	2.99	0.1446	0.7437
FACL	0.1543	87.33	1.61	2.11	0.1374	0.8695
WFCL	**0.1067**	**89.52**	**1.27**	**1.05**	**0.1448**	**0.8801**

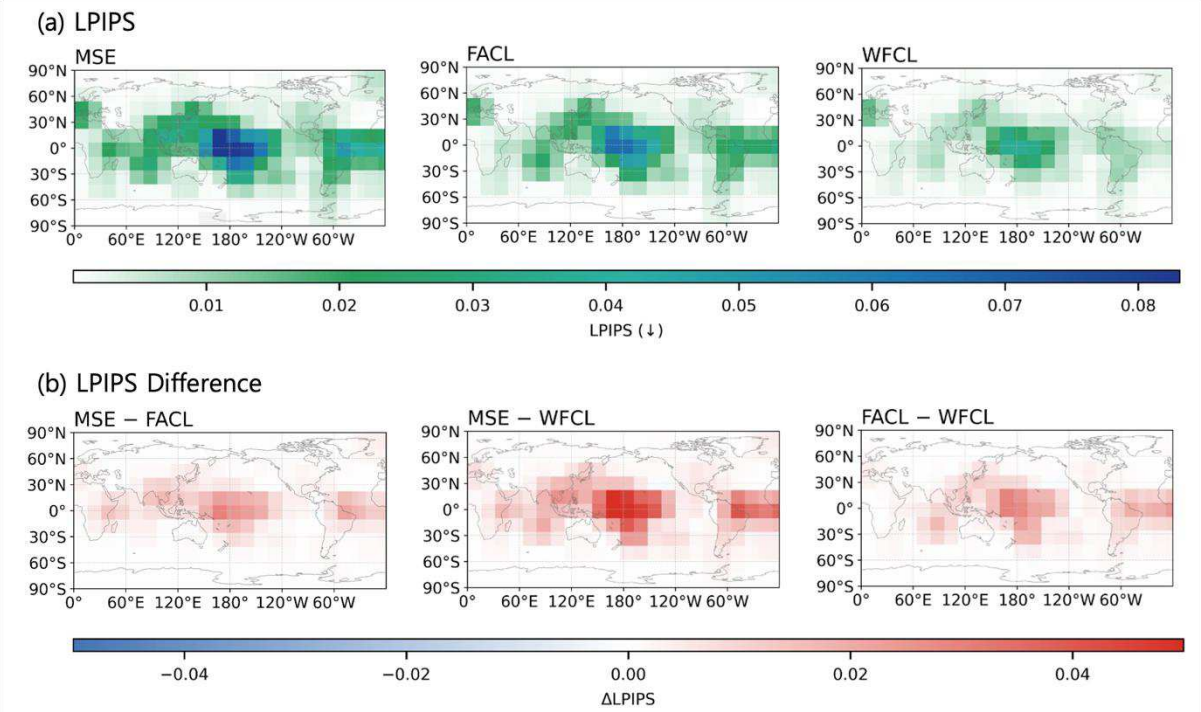


Figure 1. Comparison of perceptual differences and 1-day lead precipitation predictions between the MSE, FACL, and WFCL models for the base time of 2018-05-01. (a) Global LPIPS maps of the MSE, FACL, and WFCL models, where lower values indicate better perceptual similarity to the reference. (b) LPIPS difference maps for MSE-FACL, MSE-WFCL, and FACL-WFCL, where positive values indicate superior performance of the latter model.

Beyond perceptual metrics, we assess how the proposed loss formulation translates into physically meaningful precipitation structures at the global scale. Figure 2 presents the full global precipitation fields alongside regional insets. At the global scale, the Ground Truth exhibits zonal tropical precipitation bands and localized high-intensity features, especially over the equatorial Pacific and tropical Atlantic. Relative to the Ground Truth, the MSE-based model produces overly smoothed fields with weakened structural coherence. FACL partially improves large-scale organization but still exhibits noticeable smoothing of mesoscale features. In contrast, WFCL preserves sharper precipitation gradients and better maintains the spatial localization of intense rainfall structures across the global domain.

The regional insets make these structural differences more apparent. Over the Western–Central Tropical Pacific (130°E-210°E, 15°S-25°N; red box), WFCL better captures clustered convective cells and organized rainbands, reducing local RHD by approximately 60% relative to MSE. Over the Western North Atlantic (270°E–350°E, 10°S–30°N; green box), it more clearly resolves narrow frontal rainbands and localized intensity maxima, yielding an

approximately 40% reduction in local RHD. Together, these results indicate that WFCL enhances forecast realism by improving the spatial organization and localization of precipitation across dynamically distinct regimes.

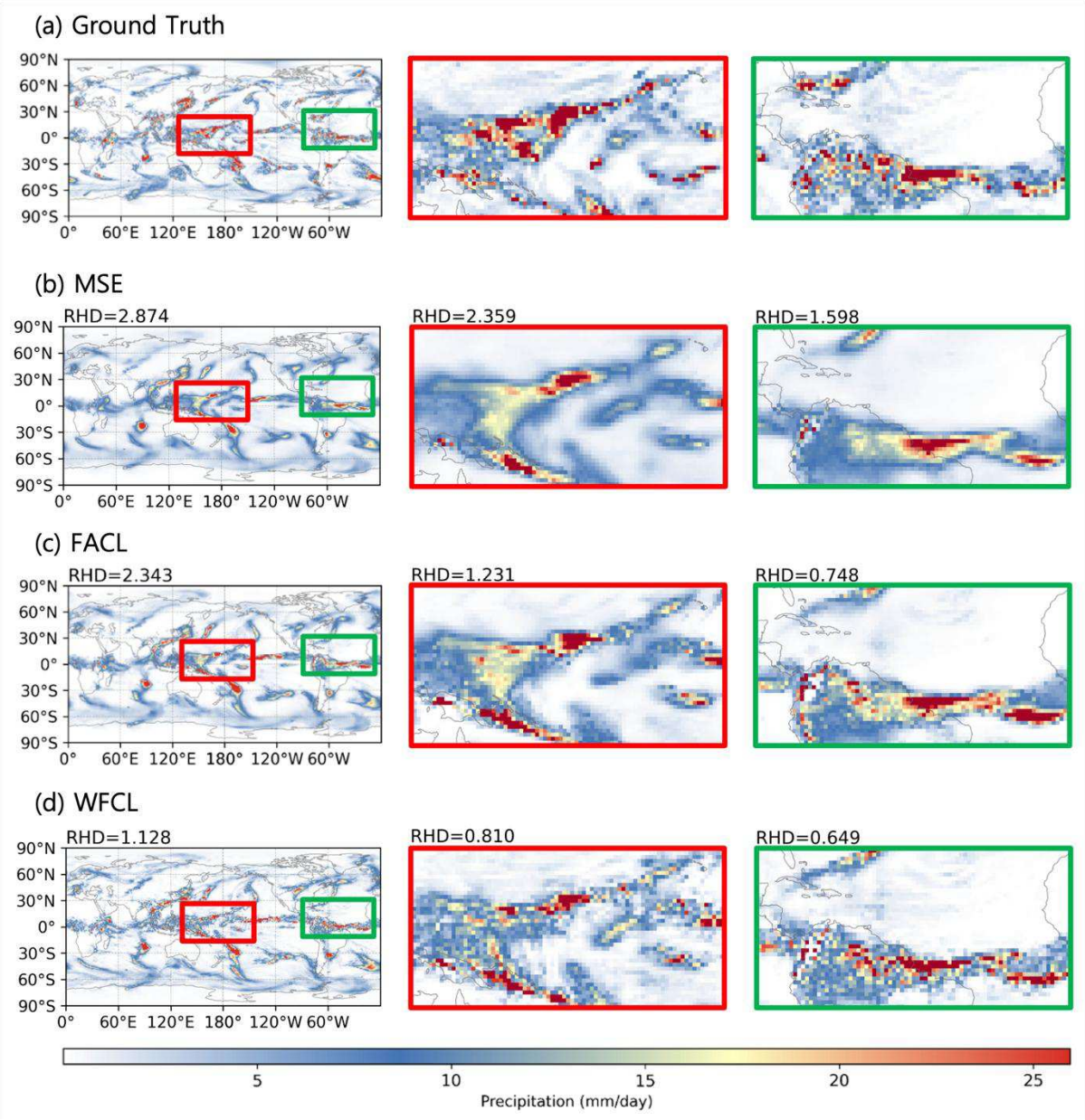


Figure 2. Comparison of 1-day lead precipitation predictions produced by different loss functions on 1 May 2018. The top row represents global precipitation fields, and the bottom row displays zoomed-in regions over the Western-Central Tropical Pacific (130°E-210°E, 15°S-25°N; red box) and the Western North Atlantic (270°E-350°E, 10°S-30°N; green box). All precipitation is expressed as daily totals (mm/day).

We next examine whether these structural enhancements are reflected in localized phase information. Figure 3a-d shows LPC patterns across three representative regions: Region 1 (30°–60°N, 70°–105°E), Region 2 (15°S–15°N, 120°–180°E), and Region 3 (15°–30°S, 80°–

105°W). In Region 1, localized phase structures that are largely suppressed in MSE and FACL are distinctly captured by WFCL. In Regions 2 and 3, the proposed model exhibits phase patterns that more closely match those of the Ground Truth than either baseline. Across all three regions, MSE and FACL show weak phase alignment and blurred boundaries, whereas WFCL preserves coherent linear features and sharp gradients. These results indicate that directional high-frequency phase information extracted by the DTCWT play a key role in representing fine-scale precipitation variability beyond what is achieved by global spectral constraints alone.

Because localized phase enhancement could potentially introduce amplitude imbalance, we further examine frequency-dependent amplitude fidelity using the radial amplitude-ratio profiles (Figure 3e), where frequency increases from low to high spatial wavenumbers. The MSE and FACL models show systematic attenuation in the mid- to high-frequency bands, consistent with their smoother spatial predictions. In contrast, WFCL maintains amplitude ratios close to 0 dB across frequencies, indicating minimal spectral distortion and improved retention of high-frequency variance associated with convective intensity. Together with the LPC results, these findings indicate that the proposed loss balances phase alignment and amplitude fidelity, enabling more accurate representation of sharp, small-scale precipitation structures.

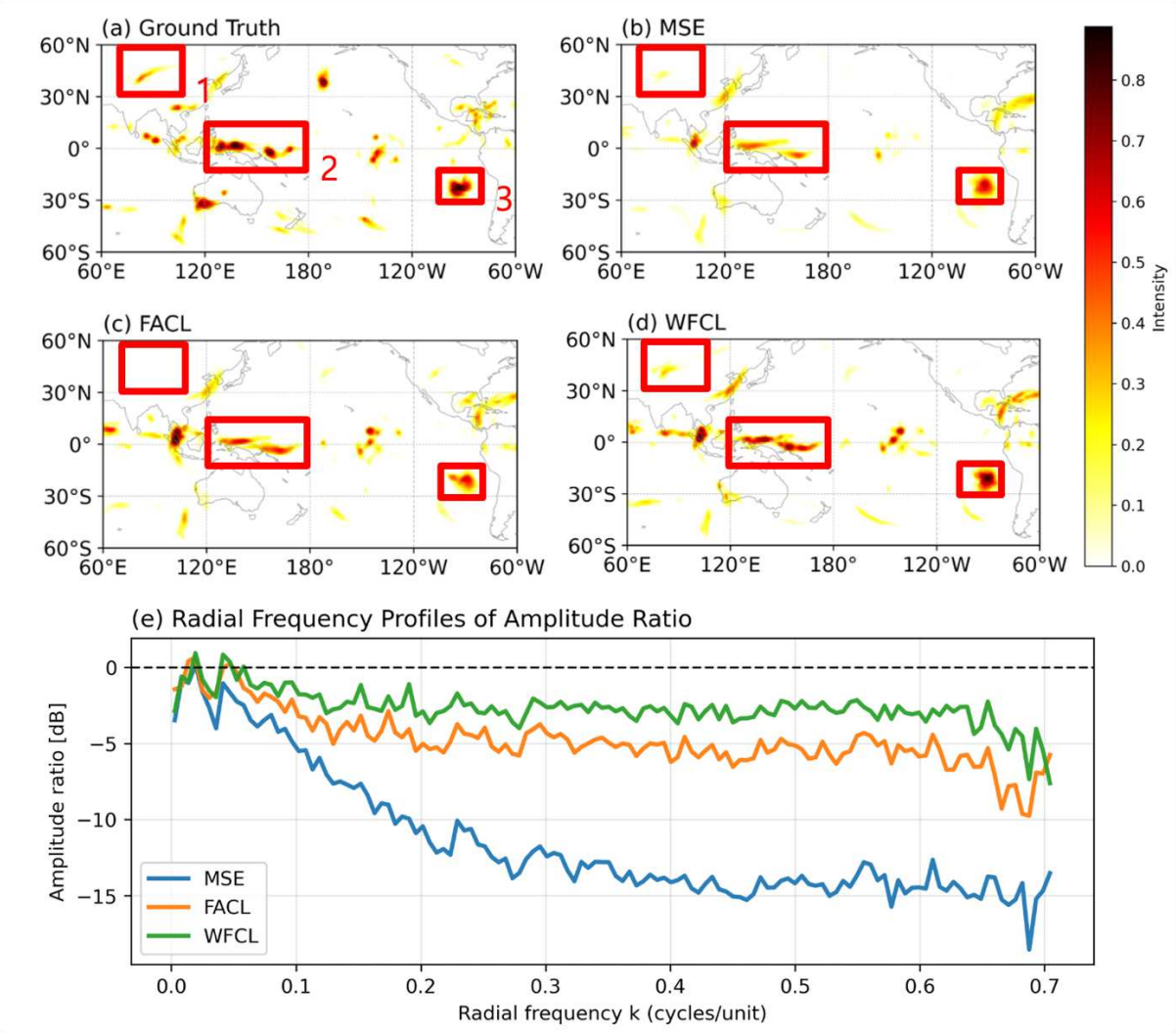


Figure 3. Comparison of predicted 1 day-lead precipitation fields across three representative regions: Region 1 (30°-60°N, 70°-105°E), Region 2 (15°S-15°N, 120°-180°E), Region 3 (15°-30°S, 80°-105°W). Panels (a-d) show the Local Phase Coherence (LPC) for each model with red boxes marking Region 1-3, and panel (e) presents their corresponding radial amplitude-ratio profiles.

Robustness of model performance across multiple lead times

WFCL consistently achieves the best performance at all lead times for LPIPS, indicating stable preservation of perceptual structure (Figure 4). The detailed spatial distributions of LPIPS at 2- and 3-day lead times, together with the inter-lead-time differences for each model, are explicitly presented in Figure S2. A similar pattern is observed for RHD and CPBD, where WFCL exhibits the slowest degradation as lead time increases, suggesting robust suppression of spatial displacement and sustained perceptual sharpness. LPC further support this stability, with WFCL sustaining superior phase alignment throughout the forecast horizon. For CSI-R95p, although MSE attains competitive scores through spatially smoothed yet stable intensity

cores, WFCL achieves comparable performance while demonstrating greater stability at longer lead times, particularly for the 3-day forecast. These results suggest that WFCL maintains extreme-event detectability without sacrificing fine-scale structural detail, mitigating the trade-off between pixel-level accuracy and structural sharpness (Yan et al., 2024). Consistently higher FSS scores for WFCL across all lead times further indicate superior precipitation coherence under spatial tolerance. Overall, WFCL delivers more stable and consistent performance across lead times than MSE and FACL by effectively balancing pixel-wise accuracy and structural realism.

Figure 5 presents a qualitative comparison across lead times for an extreme rainfall event over the middle and lower reaches of the Yangtze River during the summer of 2020, a record-breaking hydrological disaster in South-Central China (Wei et al., 2020; Jia et al., 2022). During this period, ERA5 shows daily precipitation of up to approximately 35 mm day^{-1} at 1° spatial resolution in several affected regions, indicating an exceptionally intense and spatially coherent rainfall system at the grid scale. The MSE model exhibits pronounced spatial smoothing and fails to capture both the location and intensity of observed precipitation, while FACL partially improves large-scale organization but remains affected by blurring and systematic underestimation of localized rainfall intensity. In contrast, WFCL more faithfully captures organized precipitation cells and localized intensity maxima, maintaining structural coherence and variability even at a three-day lead time despite minor displacement. A similar pattern is observed for the extreme precipitation event over the Tasman Sea and the western coast of New Zealand in July 2021 (Figure S3), reinforcing the robustness of WFCL in retaining high-frequency spatial information. These case studies emphasize the critical role of structural realism in event-scale precipitation forecasting for impact-oriented risk assessment and early warning (Zoccatelli et al., 2011; Bolla et al., 1996).

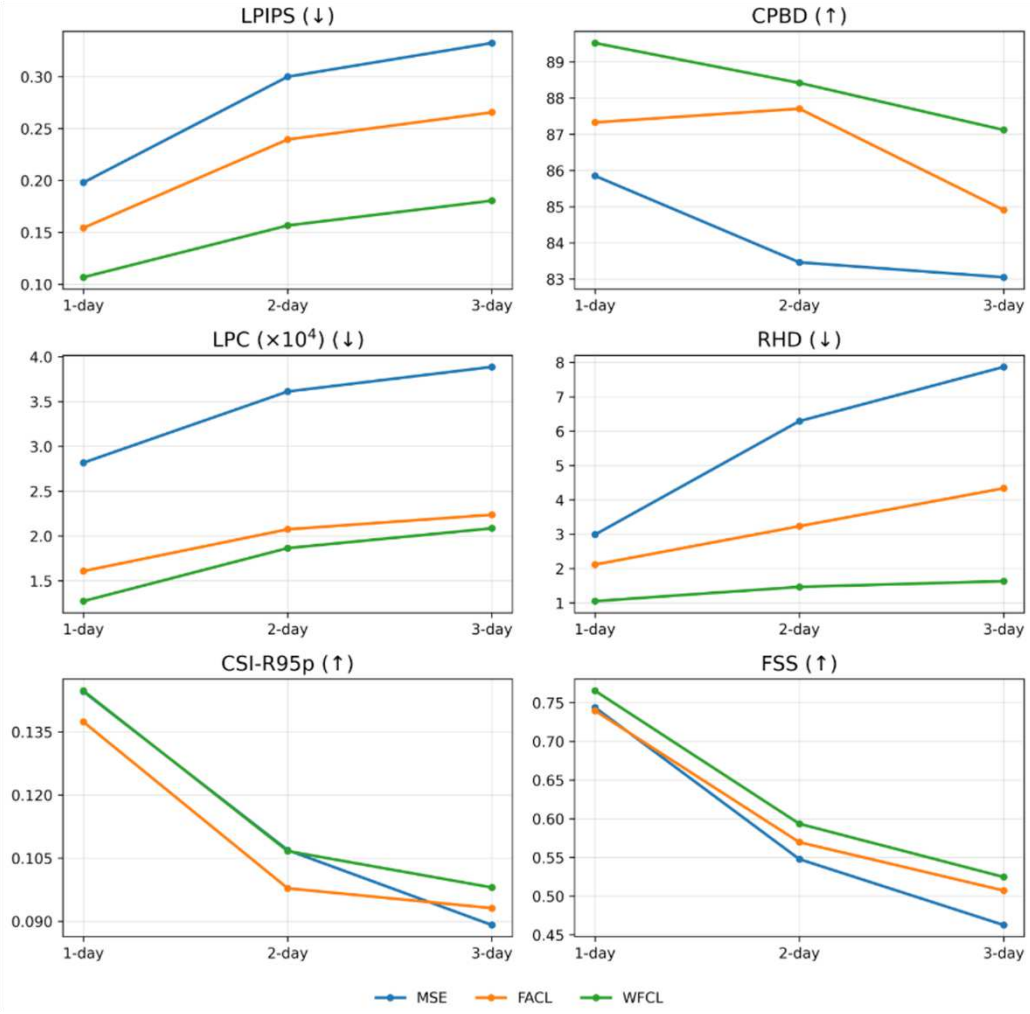


Figure 4. Performance comparison of the MSE, FACL, and WFCL models across six evaluation metrics (LPIPS, CPBD, LPC, RHD, CSI-R95p, and FSS) over lead times ranging from 1 to 3 days. The arrows in parentheses indicate the direction of performance improvement for each metric, enabling a comprehensive assessment of lead-time-dependent changes in perceptual quality, spatial error, and extreme precipitation detection skill.

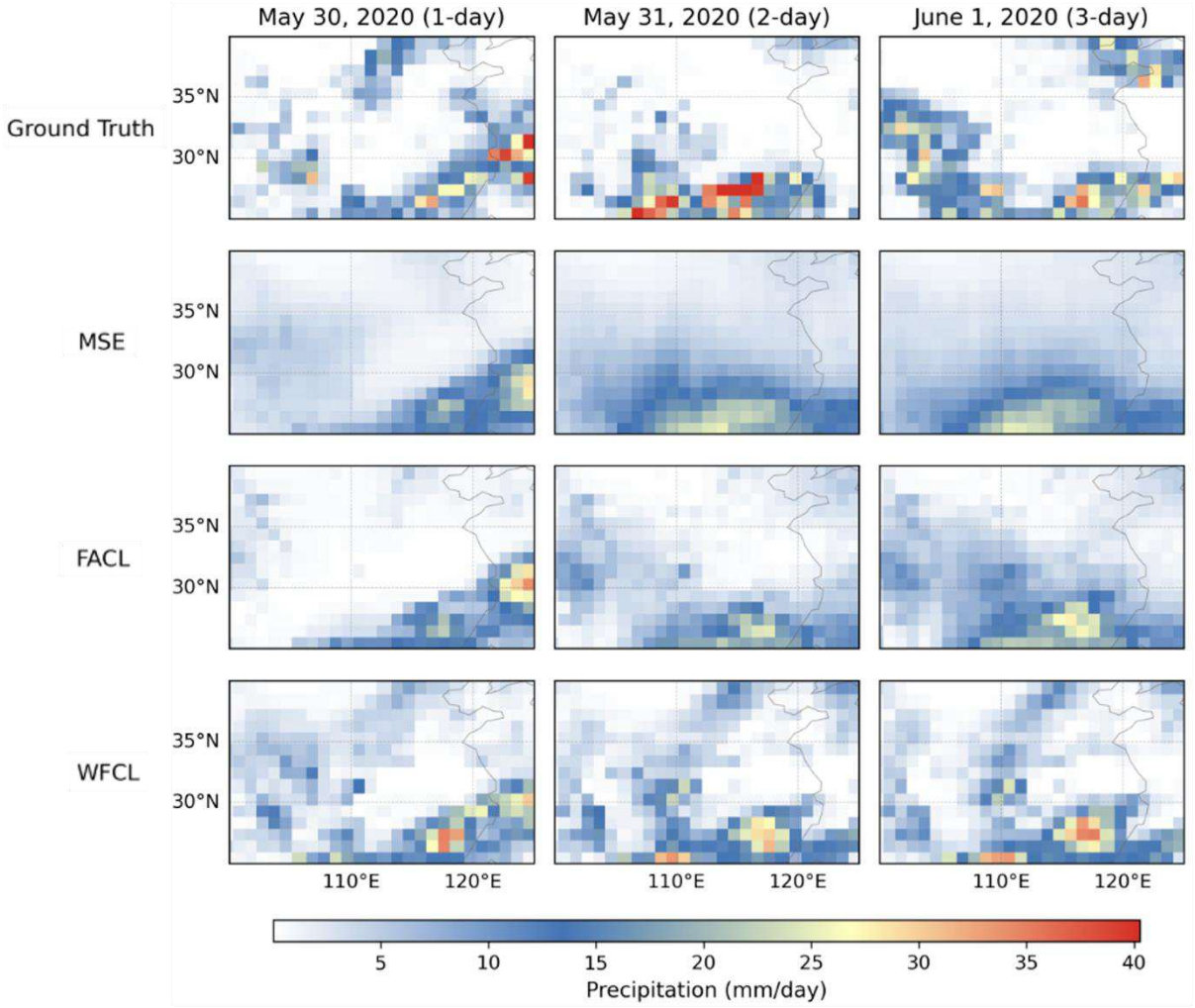


Figure 5. Comparison of predictive performance across models and lead times for the heavy precipitation event in South-Central China (100°E–125°E, 25°N–40°N) on May 29, 2020. Rows display the Ground Truth and model predictions, while columns correspond to increasing lead times.

Discussion

In this study, we propose WFCL, a structure-aware loss designed to overcome the spatial smoothing induced by MSE and the limited ability of FACL to capture localized structures. WFCL integrates FACL with WACL to jointly enforce global spectral consistency and local phase coherence. Based on global metrics averaged over 1−3day lead times, WFCL significantly improves fine-scale structural reconstruction. Quantitative analysis shows that, relative to MSE, WFCL reduces LPIPS by approximately 46%, decreases RHD by 65%, and improves CPBD by 5%, indicating an overall enhancement in perceptual quality and spatial

reconstruction. WFCL also consistently achieves lower LPC values, suggesting strengthened local phase alignment while preserving amplitude, and improved CSI-R95p scores confirm enhanced detection capability for extreme precipitation fields. A spatial-scale evaluation on 1 May 2018 further illustrates these improvements. Relative to FACL, WFCL reduces RHD by about 24% at the local scale over parts of the Pacific and Atlantic Oceans, and this localized enhancement propagates to the global scale, yielding an overall improvement of approximately 52%. These results suggest that refining local structural features directly contributes to improved global-scale spatial consistency and more physically meaningful precipitation structures.

Taken together, these results indicate that precipitation forecasting can be interpreted as a structure-constrained learning problem rather than a conventional pixel-wise regression task. WFCL explicitly separates global and local representations and decouples amplitude and phase information, enabling independent control over large-scale spectral consistency and fine-scale structural features. By elevating multi-scale local phase coherence to a primary optimization objective, the framework deliberately strengthens local structural alignment, which in turn leads to improved spatial sharpness and structural consistency across scales. This design directly addresses the fundamental limitation of grid-point intensity minimization, which often fails to capture the complex spatial dynamics of precipitation. As an architecture-agnostic mechanism implemented at the loss-function level, WFCL enforces directional and structural consistency without increasing inference complexity, offering a flexible and scalable tool for high-fidelity meteorological modeling.

Despite these advantages, emphasizing structural consistency inevitably introduces a trade-off with pixel-wise accuracy. While WFCL substantially improves spatial realism and structural coherence, improvements in displacement-sensitive pixel-based metrics may remain limited at shorter lead times. This reflects the limited tolerance of grid-point verification metrics to minor spatial shifts, where even small displacements can lead to disproportionately large penalties despite the preservation of structurally coherent precipitation patterns (Yan et al., 2024; Davis & Freeman, 1998). In this respect, conventional pixel-wise losses such as MSE remain valuable because they directly constrain grid-point intensity and positional accuracy. Notably, modern AI-based weather prediction (AIWP) models either exclude precipitation from the prognostic state variables or produce it diagnostically (Bi et al., 2023; Chen et al., 2025; Cho et al., 2026; Lang et al., 2024), partly because precipitation fields are difficult to

learn using pixel-wise losses alone. By combining the complementary strengths of MSE and WFCL, precipitation may be learned more effectively within modern AIWP frameworks. Integrating such hybrid learning objectives could enable state-of-the-art models to treat precipitation as a prognostic variable while preserving overall model performance and maintaining the characteristic behaviors of other atmospheric variables. More broadly, this capability can facilitate a more physically consistent representation of precipitation–circulation interactions, which play a central role in large scale phenomena such as monsoon systems, tropical cyclones, and organized convective events.

Methods

Data

We used the fifth-generation reanalysis from the European Centre for Medium-Range Weather Forecasts (ERA5) as the primary dataset for this study. Two predictors were extracted for model development: total precipitation (Pr) and lower-tropospheric specific humidity (Q_{low}). Q_{low} is defined as the mean specific humidity at 1000hPa and 850hPa, representing a vertically averaged moisture field in the lower troposphere. These variables were selected because lower-tropospheric humidity governs condensation, convective initiation, and large-scale moistening (Zhang et al., 2021; Kim et al., 2019; Adames et al., 2021), and exhibits strong relationships with precipitation variability, particularly during humid extremes through Clausius-Clapeyron-like scaling (Nayak et al., 2025). Precipitation itself reflects integrated microphysical and thermodynamic processes within the hydrological cycle (Surcel et al., 2017) and contains predictive information about subsequent precipitation intensity and spatial organization (Zhang et al., 2023; Waqas et al., 2024). Together, Pr and Q_{low} provide a compact predictor set that captures the key moisture supply, boundary-layer processes, and hydrological feedbacks relevant to daily precipitation variability.

For model development, we used daily ERA5 data from 1979 to 2023 and restricted the analysis to boreal summer (May-September), when precipitation and humidity variability peak in the Northern Hemisphere (Li et al., 2023). Although ERA5 is provided at a native resolution of 0.25°x0.25°, all variables were regridded to a 1°x1° global grid using bicubic interpolation to enhance computational efficiency and ensure spatial consistency (Bhattacharyya, 1969).

Finally, all predictors were standardized using z-score normalization to stabilize model optimization and align variable scales (Al-Faiz et al., 2018; Sha et al., 2020).

Model

This study employed a convolutional encoder-decoder architecture to extract multi-scale precipitation features from present-day Pr and Q_{low} (Ronneberger et al., 2015). As illustrated in Figure 6, Pr and Q_{low} were processed through two independent encoder branches, each composed of geocyclic padding followed by convolution-batch normalization-LeakyReLU (CBL) blocks. Geocyclic padding ensures spatial continuity on the global grid via latitudinal reflection and longitudinal cyclic wrapping (Cheon et al., 2024). SpatialMaxPool layers progressively reduced the spatial resolution, and the resulting feature maps were concatenated at the bottleneck.

The decoder restores the spatial resolution through upsampling and CBL blocks, with skip connections preserving fine-scale structures (Zhou et al., 2019). The decoder output is reshaped along a synthetic temporal axis and passed through 3D convolutional layers to produce 1-, 2-, 3-day precipitation forecasts. LeakyReLU activations and dropout are applied throughout the encoder-decoder to enhance nonlinear representation and model generalization (Demir & Yilmaz, 2020; Xing et al., 2022; Mastromichalakis, 2023). The model is trained using the Adam optimizer with a learning rate of 10^{-4}, 80 training epochs, and a batch size of 16. These hyperparameters were determined empirically, and the model exhibited low sensitivity to their variation, with convergence occurring well before 100 epochs. Learned Perceptual Image Patch Similarity (LPIPS), which evaluates perceptual similarity based on deep feature representations rather than pixel-wise errors, is particularly suitable for capturing structurally relevant precipitation patterns; therefore, the final model configuration was selected according to the best LPIPS score (Zhang et al., 2018; Seal et al., 2024).

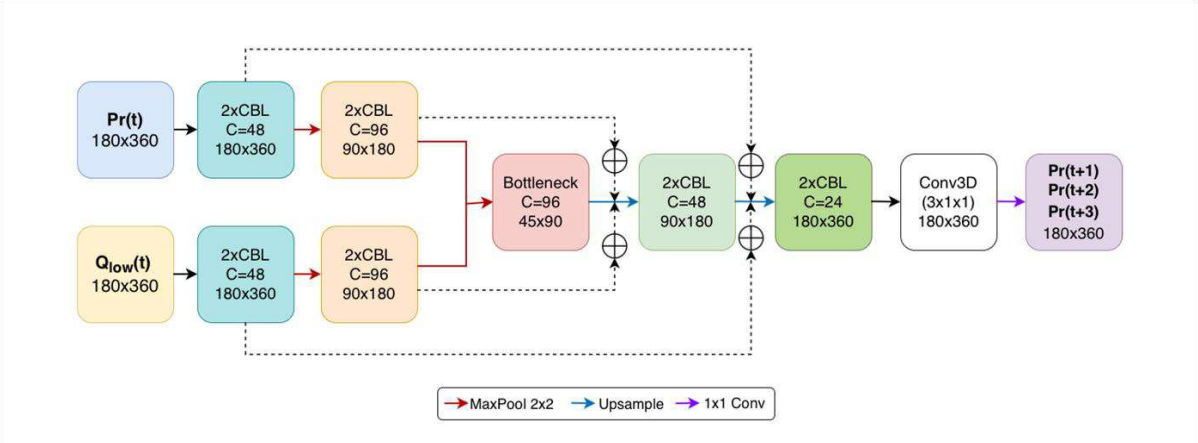


Figure 6. Architecture of the U-Net based precipitation prediction model for 1-3-day lead time forecasting.

Loss function

Frequency- and Scale-aware Representations

To address the limitation caused by the conventional pixel-wise loss function (e.g., MSE), we designed a loss function that incorporated frequency- and scale-aware representations, enabling the training under explicit constrains that capture both global spectral organization and localized structural variability in precipitation fields.

The Fourier transform provides a global frequency-domain representation for precipitation fields by decomposing spatial patterns into amplitude and phase components (Yan et al., 2024). Using a Discrete Fourier Transform (DFT), a precipitation field Pr(t+k) was mapped to the frequency domain and represented by its real and imaginary components, denoted as F_{real} and F_{imag}. The amplitude spectrum is defined as $|F| = \sqrt{F_{real}^2 + F_{imag}^2}$ and characterizes the distribution of spectral energy across spatial scales, while the phase information, defined as $\theta_F = \arctan(\frac{F_{imag}}{F_{real}})$, governs the spatial alignment and coherence of precipitation structures (Figure 7a). By jointly constraining amplitude and phase, FACL preserves spectral energy through an amplitude-matching term (FAL) and maintain phase coherence via a normalized Fourier-domain correlation term (FCL).

Specifically, the FAL penalizes discrepancies between the predicted and reference amplitude spectra:

$$FAL(X, \hat{X}) = \frac{1}{MN} \sum_{p,q} \left(|F|_{pq} - |\hat{F}|_{pq} \right)^2 \quad (1)$$

where p and q denote the vertical and horizontal frequency indices spanning the $M \times N$ Fourier grid. Phase alignment is enforced by the FCL:

$$FCL(X, \hat{X}) = 1 - \frac{\sum \Re(F\hat{F}^*)}{\sqrt{\sum |F|^2 \sum |\hat{F}|^2}} \quad (2)$$

which measures normalized complex correlation in the Fourier domain. Here, $(\cdot)^*$ denotes the complex conjugate and $\Re(\cdot)$ extracts the real part. However, because the DFT represents the entire spatial field in a global frequency domain by assuming the stationarity, it lacks spatial locality which limits its ability to represent localized or direction-dependent structures (Pineda et al., 2008; Yang & Guan, 2026; Abrahamsen et al., 2018; Ni et al., 2024), thereby motivating the incorporation of complementary scale-aware representations.

Wavelet-based approaches provide a complementary representation by enabling localized and spatially varying analysis of precipitation fields. Unlike global Fourier representations, wavelet transforms jointly resolve spatial and scale information, allowing localized, multi-scale structures to be explicitly characterized. A real-valued Discrete Wavelet Transform (DWT) offers multi-scale decomposition but lacks a coherent amplitude–phase representation and exhibits limited directional selectivity, which constrains its ability to capture orientation-dependent precipitation features (Kingsbury, 2000; Fernandes et al., 2000).

To overcome these limitations, we employed the Dual-Tree Complex Wavelet Transform (DTCWT) (Kingsbury, 1998), which yields complex-valued coefficients with explicit local amplitude and phase information and enhanced directional selectivity. The transform consists of two parallel filter banks (Tree a and Tree b) forming approximate Hilbert pairs, where Tree b is a half-sample shifted and approximately 90° phase-rotated relative to Tree a (Kingsbury, 1999; Figure 7b). Within each tree, a pair of low-pass and high-pass filters decomposes the signal into smooth, slowly varying components and rapidly varying oscillatory responses, respectively. By combining the high-pass outputs from both trees, complex wavelet coefficients are formed as $w_\theta = w_{\theta,a} + jw_{\theta,b}$, where $w_{\theta,a}$ and $w_{\theta,b}$ denote the real-valued coefficients from Tree a and Tree b, respectively. The corresponding local amplitude and phase are defined as $|W| = \sqrt{w_a^2 + w_b^2}$ and $\theta_W = \arctan\left(\frac{w_b}{w_a}\right)$, enabling explicit characterization of localized, orientation-dependent structures. For two-dimensional inputs, the DTCWT decomposes the precipitation field into one low-frequency sub-band and six oriented high-

frequency sub-bands (i.e., ±15°, ±45°, ±75°), yielding a directionally enriched multi-scale representation (Hill et al., 2015; Singh et al., 2014).

When extended across multiple decomposition levels, the directional decomposition is recursively applied only to the low-frequency sub-band generated at the previous stage, forming a hierarchical multiscale representation through successive filter-bank operations. At each level, six new directional high-frequency sub-bands are produced, while the previously extracted high-frequency bands are retained. Although the same filter pairs are applied at every level, the effective spatial resolution decreases due to successive down-sampling. Consequently, the filters operate over progressively larger spatial windows, enabling deeper levels to capture relatively lower-frequency structures. As the decomposition proceeds, the effective frequency support progressively narrows and shifts toward lower central frequencies (Selesnick et al., 2005). As a result, higher-level high-frequency components increasingly reflect organized mesoscale structures rather than grid-scale fluctuations, enabling directional organization to be examined consistently across spatial scales (Figure S1).

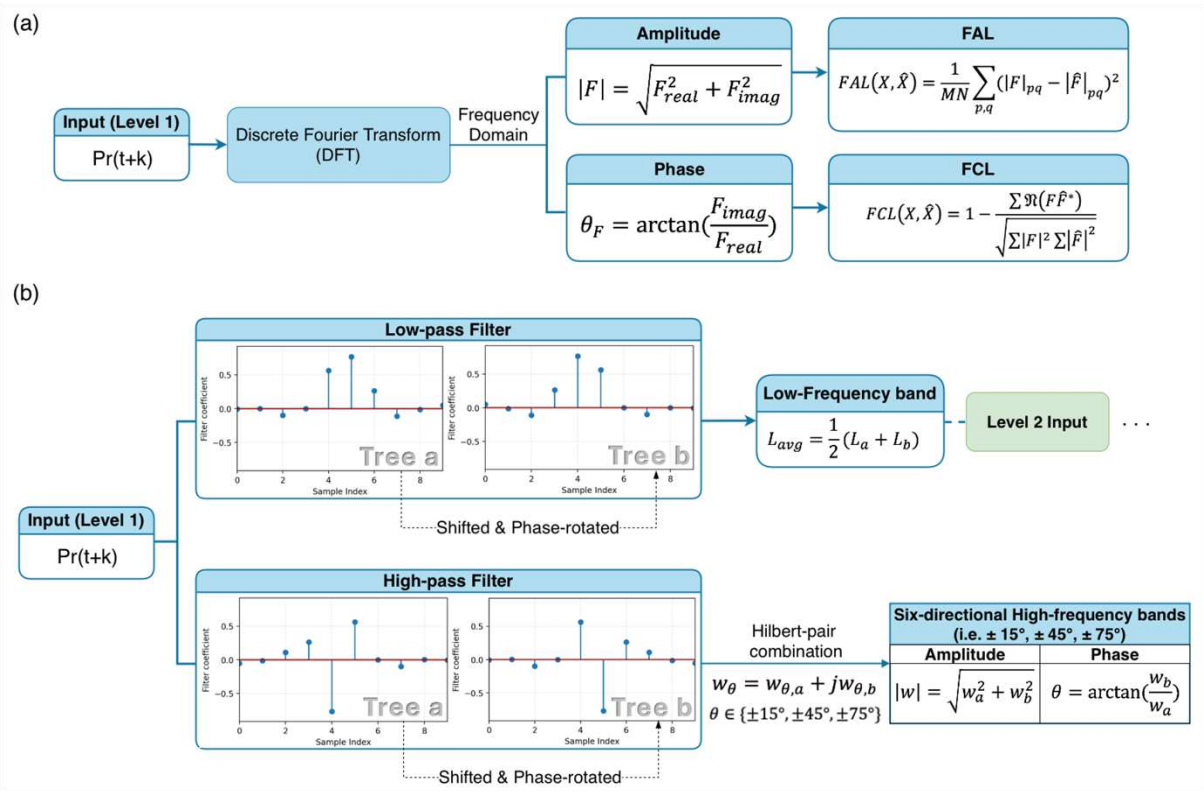


Figure 7. (a) Fourier Amplitude and Correlation Loss (FACL) framework: Discrete Fourier Transform (DFT)-based spectral decomposition into amplitude and phase components constrained by the Fourier Amplitude Loss (FAL) and Fourier Correlation Loss (FCL) (see Eqs. (1–2)). (b) Level-1 Dual-Tree Complex Wavelet Transform (DTCWT), consisting of two

parallel filter banks (Tree a and Tree b) forming approximate Hilbert pairs. Their outputs w_a and w_b form the complex coefficient $w_\theta = w_{\theta,a} + jw_{\theta,b}$ ($\theta \in \{\pm 15°, \pm 45°, \pm 75°\}$), providing localized amplitude-phase representation.

Proposed loss function: Wavelet-Fourier Composite Loss

To jointly constrain global spectral organization and localized, scale-dependent structure in precipitation fields, we formulated a composite loss function that integrates Fourier- and wavelet-based constraints. Two complementary wavelet-based loss components, the Wavelet Amplitude Loss (WAL) and the Wavelet Correlation Loss (WCL), were defined on the complex DTCWT coefficient $H^{(L,k)}$, where $H^{(L,k)}$ denotes the complex-valued coefficient at decomposition level L and the k-th directional band obtained from the target and predicted precipitation fields X and $\hat{X}$.

The WAL penalizes discrepancies in the magnitude,

$$WAL^{(L,k)}(X,\hat{X}) = \frac{1}{MN}\sum_{p,q}\left(\left|H_{pq}^{(L,k)}\right| - \left|\hat{H}_{pq}^{(L,k)}\right|\right)^2 \tag{3}$$

where $M \times N$ denotes the spatial dimensions of the corresponding directional band. To preserve localized phase alignment, the WCL is defined using a normalized complex correlation,

$$WCL^{(L,k)}(X,\hat{X}) = 1 - \frac{\sum \Re\left(H^{(L,k)}\hat{H}^{(L,k)^*}\right)}{\sqrt{\sum|H^{(L,k)}|^2}\sqrt{\sum\left|\hat{H}^{(L,k)}\right|^2} + \varepsilon} \tag{4}$$

where ε is a small constant for numerical stability. The WAL and WCL are combined to form the Wavelet Amplitude and Correlation Loss (WACL),

$$WACL_{\mathbb{E}}^{(L,k)}(X,\hat{X}) = (1-P_t)\,WAL^{(L,k)}(X,\hat{X}) + P_t\,WCL^{(L,k)}(X,\hat{X}) \tag{5}$$

where the scheduling parameter P_t balances amplitude- and phase-based constraints during training. To stabilize optimization, we adopt a linear scheduling strategy,

$$P_t = \max\left(0, 1 - \frac{t}{(1-\alpha)T}\right), \qquad \alpha = 0.1 \tag{6}$$

with t denoting the current training step and T the total number of training steps.

The final loss combines the proposed WACL with the FACL to couple global Fourier-domain consistency with localized wavelet-domain constraints. FACL stabilizes large-scale precipitation structures, whereas WACL operates on the six directional high-frequency DTCWT bands at each level L, enhancing sharp boundaries, directional structures, and fine-scale convective features. The per-level weights γ_L modulate the relative importance of each wavelet level and were normalized to ensure balanced supervision across scales. The final loss was defined as

$$\mathcal{L}_{total}^{(\mathbb{E})} = \beta FACL_{\mathbb{E}}(X, \hat{X}) + \sum_{L=1}^{J} \frac{\gamma_L}{6} \sum_{k=1}^{6} WACL_{\mathbb{E}}^{(L,k)}(X, \hat{X}) \quad (7)$$

where β controls the contribution of the global component. In this study, β was set to 1 to ensure equal weighting between the global FACL term and the local WACL terms. Since global structural characteristics are already captured by the FACL component, the low-frequency wavelet band was excluded from the loss formulation. The loss was therefore computed using only the six directional high-frequency wavelet bands, assigning equal weights to avoid emphasizing any specific orientation during training, and the factor 1/6 normalizes their aggregated contribution at each decomposition level. Based on previous studies reporting that increasing decomposition depth consistently improves structural and perceptual metrics with only marginal degradation in Local Phase Coherence, indicating a well-balanced trade-off between pixel-wise error and spatial skill (Yan et al., 2024), we adopted WFCL Level 3 as the final model configuration in this study.

Evaluation

This study evaluated the impact of different loss functions on precipitation prediction performance by comparing models trained with MSE, FACL, and the proposed WFCL. To ensure a fair comparison, all experiments employed the same U-Net architecture (Figure 1), differing only in the choice of loss function. The model was trained using data from 1979−2015, validated on 2016−2017, and evaluated on an independent test set covering 2018−2023.

Model performance was assessed using a suite of complementary metrics capturing perceptual and structural fidelity, spatial localization, extreme-event detection, and spatial forecast skill. Perceptual and structural similarity was measured by LPIPS, Cumulative Probability of Blur Detection (CPBD), and Local Phase Coherence (LPC). Spatial localization

performance was quantified using Regional Histogram Divergence (RHD), extreme precipitation detection skill was assessed using the Critical Success Index for 95th percentiles (CSI-R95p), and spatial forecast skill was evaluated using the Fractions Skill Score (FSS) (Zhang et al., 2018; Narvekar & Karam, 2011; Wang & Simoncelli, 2003; Yan et al., 2024; Schaefer, 1990; Roberts & Lean, 2008). Mathematical definitions of all evaluation metrics are provided in Supplementary Note 1. These metrics are widely adopted in precipitation forecasting studies to assess performance from multiple perspectives. Scale-dependent spectral behavior was additionally examined using radial amplitude ratios derived from 2D Fast Fourier Transform magnitudes, leveraging the FFT for computational efficiency in evaluating the Discrete Fourier Transform.

Acknowledgments

This research was supported by the ASTRA Project through the National Research Foundation (NRF) funded by the Ministry of Science and ICT (No. RS-2024-00440482).

Data availability

The datasets used in this study were obtained from the ERA5 reanalysis archive and are publicly available at https://www.ecmwf.int/en/forecasts/dataset/ecmwf-reanalysis-v5.

Code availability

The code used for analysis in this study is available from the corresponding author upon reasonable request.

Author contributions

S. An contributed to data curation, methodology development, formal analysis, and wrote the manuscript. Y. Kim contributed to data curation, methodology development, and formal analysis. D. Cho contributed to data curation, conceptualization, and modeling, and wrote, reviewed, and edited the manuscript. Y. Ham contributed to conceptualization, supervised the project, provided resources, reviewed and edited the manuscript, and acquired funding. All authors discussed the results and reviewed and approved the final manuscript.

Competing interests

I declare that the authors have no competing interests as defined by Nature Portfolio, or other interests that might be perceived to influence the results and/or discussion reported in this paper.

References

Abbas, A., & Tran, T. D. (2008). Rational coefficient dual-tree complex wavelet transform: Design and implementation. *IEEE Transactions on Signal Processing, 56*(8), 3523–3534. https://doi.org/10.1109/TSP.2008.925898

Abbas, M., Zhao, L., & Wang, Y. (2022). Perspective impact on water environment and hydrological regime owing to climate change: A review. *Hydrology, 9*(11), 203. https://doi.org/10.3390/hydrology9110203

Abrahamsen, P., Kvernelv, V., & Barker, D. (2018). Simulation of Gaussian random fields using the fast Fourier transform (FFT). In *ECMOR XVI—16th European Conference on the Mathematics of Oil Recovery*. https://doi.org/10.3997/2214-4609.201802134

Adames, Á. F., Powell, S. W., Ahmed, F., Mayta, V. C., & Neelin, J. D. (2021). Tropical precipitation evolution in a buoyancy-budget framework. *Journal of the Atmospheric Sciences, 78*(2), 509–528. https://doi.org/10.1175/JAS-D-20-0074.1

Al-Faiz, M. Z., Ibrahim, A. A., & Hadi, S. M. (2018). The effect of Z-score standardization (normalization) on binary input due the speed of learning in back-propagation neural network. *Iraqi Journal of Information and Communication Technology, 1*(3), 42–48. https://doi.org/10.31987/ijict.1.3.41

Bannister, R. N., Chipilski, H. G., & Martinez-Alvarado, O. (2020). Techniques and challenges in the assimilation of atmospheric water observations for numerical weather prediction towards convective scales. *Quarterly Journal of the Royal Meteorological Society, 146*(726), 1–48. https://doi.org/10.1002/qj.3652

Bhattacharyya, B. K. (1969). Bicubic spline interpolation as a method for treatment of potential field data. *Geophysics, 34*(3), 402–423. https://doi.org/10.1190/1.1440019

Bi, K., Xie, L., Zhang, H., Chen, X., Gu, X., & Tian, Q. (2023). Accurate medium-range global weather forecasting with 3D neural networks. *Nature, 619*(7970), 533–538. https://doi.org/10.1038/s41586-023-06185-3

Bolla, R., Boni, G., La Barbera, P., Lanza, L., Marchese, M., & Zappatore, S. (1996). The tracking and prediction of high intensity rainstorms. *Remote Sensing Reviews, 14*(1–3), 151–183. https://doi.org/10.1080/02757259609532316

Caelli, T., & Bevan, P. (1982). Visual sensitivity to two-dimensional spatial phase. *Journal of the Optical Society of America, 72*(10), 1375–1381. https://doi.org/10.1364/JOSA.72.001375

Cao, Y., Li, S., Feng, J., Chen, L., Li, H., & Zhang, Y. (2025). Enhancing machine learning models for nowcasting and short-term forecasting of precipitation with a novel probability-matching loss function. *Geophysical Research Letters, 52*(24), e2025GL119442. https://doi.org/10.1029/2025GL119442

Chen, G., & Wang, W. C. (2022). Short-term precipitation prediction for contiguous United States using deep learning. *Geophysical Research Letters, 49*(8), e2022GL097904. https://doi.org/10.1029/2022GL097904

Chen, K., Han, T., Ling, F., Gong, J., Bai, L., Wang, X., ... & Ouyang, W. (2025). The operational medium-range deterministic weather forecasting can be extended beyond a 10-day lead time. *Communications Earth & Environment, 6*(1), 518. https://doi.org/10.1038/s43247-025-02502-y

Chen, S. S., & Houze Jr, R. A. (1997). Diurnal variation and life-cycle of deep convective systems over the tropical Pacific warm pool. *Quarterly Journal of the Royal Meteorological Society, 123*(538), 357–388. https://doi.org/10.1002/qj.49712353806

Chen, X., Wang, M., Wang, S., Chen, Y., Wang, R., Zhao, C., & Hu, X. (2022). Weather radar nowcasting for extreme precipitation prediction based on the temporal and spatial generative adversarial network. *Atmosphere, 13*(8), 1291. https://doi.org/10.3390/atmos13081291

Cheon, M., Choi, Y. H., Kang, S. Y., Choi, Y., Lee, J. G., & Kang, D. (2024). Karina: An efficient deep learning model for global weather forecast. *arXiv preprint*. https://doi.org/10.48550/arXiv.2403.10555

Cho, D., Ham, Y. G., Jeong, S., & Kang, S. Y. (2026). A deep learning-based land-atmosphere coupled model for heatwave prediction. *npj Climate and Atmospheric Science*. https://doi.org/10.1038/s41612-025-01311-6

Davis, C. Q., & Freeman, D. M. (1998). Statistics of subpixel registration algorithms based on spatiotemporal gradients or block matching. *Optical Engineering, 37*(4), 1290–1298. https://doi.org/10.1117/1.601966

DEMİR, A., & Yilmaz, F. (2020). Inception-ResNet-v2 with LeakyReLU and average pooling for more reliable and accurate classification of chest X-ray images. In *Medical Technologies Congress*. https://doi.org/10.1109/TIPTEKNO50054.2020.9299232

Duncan, J., Subramanian, S., & Harrington, P. (2022). Generative modeling of high-resolution global precipitation forecasts. *arXiv preprint*. https://doi.org/10.48550/arXiv.2210.12504

Fernandes, F., van Spaendonck, R., Coates, M. J., & Burrus, C. S. (2000). Directional complex-wavelet processing. In *Wavelet Applications in Signal and Image Processing VIII*. https://doi.org/10.1117/12.408642

Guilloteau, C., & Foufoula-Georgiou, E. (2023). Preserving extremes in satellite quantitative precipitation estimates: A matter of scale. In *IGARSS 2023*. https://doi.org/10.1109/IGARSS52108.2023.10281499

Ham, Y. G., Kim, J. H., Min, S. K., Kim, D., Li, T., Timmermann, A., & Stuecker, M. F. (2023). Anthropogenic fingerprints in daily precipitation revealed by deep learning. *Nature, 622*(7982), 301–307. https://doi.org/10.1038/s41586-023-06474-x

Hill, P. R., Anantrasirichai, N., Achim, A., Al-Mualla, M. E., & Bull, D. R. (2015). Undecimated dual-tree complex wavelet transforms. *Signal Processing: Image Communication, 35*, 61–70. https://doi.org/10.1016/j.image.2015.04.010

Houze Jr, R. A., Chen, S. S., Kingsmill, D. E., Serra, Y., & Yuter, S. E. (2000). Convection over the Pacific warm pool in relation to the atmospheric Kelvin–Rossby wave. *Journal of the Atmospheric Sciences, 57*(18), 3058–3089. https://doi.org/10.1175/1520-0469(2000)057<3058:COTPWP>2.0.CO;2

Hrour, Y., Thomas, Z., Fovet, O., Rousseau-Gueutin, P., Pichelin, P., & Sebari, K. (2020). Precipitation trends and ruptures effect on catchment hydrology and water resources availability for agricultural lands under climate change. *EGU General Assembly Conference Abstracts*. https://doi.org/10.5194/egusphere-egu2020-11333

IPCC. (2021). *Climate change 2021: The physical science basis*. Cambridge University Press. https://doi.org/10.1017/9781009157896

Jia, H., Chen, F., Pan, D., Du, E., Wang, L., Wang, N., & Yang, A. (2022). Flood risk management in the Yangtze River basin—Comparison of 1998 and 2020 events. *International Journal of Disaster Risk Reduction, 68*, 102724. https://doi.org/10.1016/j.ijdrr.2021.102724

Kazheen S. Muhammad, & Omar Sedqi Kareem. (2025). A comparative study of data mining algorithms for weather prediction. *Engineering and Technology Journal, 10*(5), 5186–5191. https://doi.org/10.47191/etj/v10i05.47

Kim, J. Y., & Kim, K. Y. (2019). Relative role of horizontal and vertical processes in the physical mechanism of wintertime Arctic amplification. *Climate Dynamics, 52*(9), 6097–6107. https://doi.org/10.1007/s00382-018-4499-2

Kingsbury, N. (1998). The dual-tree complex wavelet transform: A new efficient tool for image restoration and enhancement. *European Signal Processing Conference*.

Kingsbury, N. (1999). Shift invariant properties of the dual-tree complex wavelet transform. In *ICASSP*. https://doi.org/10.1109/ICASSP.1999.756198

Kingsbury, N. (2000). A dual-tree complex wavelet transform with improved orthogonality and symmetry properties. In *International Conference on Image Processing*. https://doi.org/10.1109/ICIP.2000.899397

Lang, S., Alexe, M., Chantry, M., Dramsch, J., Pinault, F., Raoult, B., ... & Rabier, F. (2024). AIFS—ECMWF's data-driven forecasting system. *arXiv preprint*. https://doi.org/10.48550/arXiv.2406.01465

Lee, S. S., Li, Z., Zhang, Y., Yoo, H., Kim, S., Kim, B. G., ... & Dong, D. (2018). Effects of model resolution and parameterizations on the simulations of clouds, precipitation, and their interactions with aerosols. *Atmospheric Chemistry and Physics, 18*(1), 13–29. https://doi.org/10.5194/acp-18-13-2018

Leelawat, N., Laosunthara, A., Srivichai, M., Sararit, T., Kodaka, A., Tungkasikij, N., ... & Tang, J. (2025). The 2024 Northern Thailand floods: A preliminary disaster report. *Journal of Disaster Research*. https://doi.org/10.20965/jdr.2025.sc20250319

Li, J., Shi, Y., Zhang, T., Li, Z., Wang, C., & Liu, J. (2024). Radar precipitation nowcasting based on ConvLSTM model in a small watershed in north China. *Natural Hazards, 120*(1), 63–85. https://doi.org/10.1007/s11069-023-06193-6

Li, Y., Gong, H., Chen, W., Wang, L., Wu, R., Dong, Z., ... & Ma, K. (2023). Summer precipitation variability in the Mongolian Plateau and its possible causes. *Global and Planetary Change, 228*, 104189. https://doi.org/10.1016/j.gloplacha.2023.104189

Liu, H., Fung, J. C., Lau, A. K., & Li, Z. (2024). Enhancing quantitative precipitation estimation of NWP model with fundamental meteorological variables and transformer-based deep learning model. *Earth and Space Science, 11*(4), e2023EA003234. https://doi.org/10.1029/2023EA003234

Marengo, J. A., Ambrizzi, T., Alves, L. M., Barreto, N. J., Simões Reboita, M., & Ramos, A. M. (2020). Changing trends in rainfall extremes in the metropolitan area of São Paulo: Causes and impacts. *Frontiers in Climate, 2*, 3. https://doi.org/10.3389/fclim.2020.00003

Mohr, S., Ehret, U., Kunz, M., Ludwig, P., Caldas-Alvarez, A., Daniell, J. E., ... & Wisotzky, C. (2022). A multi-disciplinary analysis of the exceptional flood event of July 2021 in central Europe. Part 1: Event description and analysis. *Natural Hazards and Earth System Sciences*. https://doi.org/10.5194/nhess-23-525-2023

Muller, C., & Takayabu, Y. (2020). Response of precipitation extremes to warming. *Environmental Research Letters, 15*(3), 035001. https://doi.org/10.1088/1748-9326/ab7130

Narvekar, N. D., & Karam, L. J. (2011). A no-reference image blur metric based on the cumulative probability of blur detection. *IEEE Transactions on Image Processing, 20*(9), 2678–2683. https://doi.org/10.1109/TIP.2011.2131660

Nazeri Tahroudi, M. (2025). Comprehensive global assessment of precipitation trend and pattern variability. *Scientific Reports, 15*(1), 22458. https://doi.org/10.1038/s41598-025-06050-5

Ni, Z., Wu, J., Wang, Z., Yang, W., Wang, H., & Ma, L. (2024). Misalignment-robust frequency distribution loss for image transformation. In *CVPR 2024*. https://doi.org/10.1109/CVPR52733.2024.00281

Pedder, M. A., Haile, M., & Thorpe, A. J. (2000). Short period forecasting of catchment-scale precipitation. *Hydrology and Earth System Sciences, 4*(4), 627–633. https://doi.org/10.5194/hess-4-627-2000

Ravuri, S., Lenc, K., Willson, M., Kangin, D., Lam, R., Mirowski, P., ... & Mohamed, S. (2021). Skilful precipitation nowcasting using deep generative models of radar. *Nature, 597*(7878), 672–677. https://doi.org/10.1038/s41586-021-03854-z

Roberts, N. M., & Lean, H. W. (2008). Scale-selective verification of rainfall accumulations from high-resolution forecasts of convective events. *Monthly Weather Review, 136*(1), 78–97. https://doi.org/10.1175/2007MWR2123.1

Ronneberger, O., Fischer, P., & Brox, T. (2015). U-net: Convolutional networks for biomedical image segmentation. https://doi.org/10.48550/arXiv.1505.04597

Sadeghi, M., Asanjan, A. A., Faridzad, M., Nguyen, P. H. U., Hsu, K., Sorooshian, S., & Braithwaite, D. (2019). PERSIANN-CNN. *Journal of Hydrometeorology, 20*(12), 2273–2289. https://doi.org/10.1175/JHM-D-19-0110.1

Schaefer, J. T. (1990). The critical success index as an indicator of warning skill. *Weather and Forecasting, 5*(4), 570–575.

Seal, D., Arcucci, R., Rühling-Cachay, S., & Quilodrán-Casas, C. (2024). DYffCast. *arXiv preprint*. https://doi.org/10.48550/arXiv.2412.02723

Selesnick, I. W., Baraniuk, R. G., & Kingsbury, N. C. (2005). The dual-tree complex wavelet transform. *IEEE Signal Processing Magazine, 22*(6), 123–151. https://doi.org/10.1109/MSP.2005.1550194

Shi, C., Xu, H., Li, Y., Wei, Y. L., Feng, Y., Zhang, Y., & Niu, D. (2025). WaveC2R. *arXiv preprint*. https://doi.org/10.48550/arXiv.2511.17558

Shi, X., Chen, Z., Wang, H., Yeung, D. Y., Wong, W. K., & Woo, W. C. (2015). Convolutional LSTM network. *Advances in Neural Information Processing Systems*. https://doi.org/10.48550/arXiv.1506.04214

Singh, H., Kaur, L., & Singh, K. (2014). Fractional M-band dual tree complex wavelet transform for digital watermarking. *Sadhana, 39*(2), 345–361. https://doi.org/10.1007/s12046-013-0217-2

Staal, A., & Koren, G. (2023). Comment on 'The central role of forests in the 2021 European floods'. *Environmental Research Letters, 18*(4), 048002. https://doi.org/10.1088/1748-9326/acc260

Surcel, M., Zawadzki, I., Yau, M. K., Xue, M., & Kong, F. (2017). Scale dependence of the predictability of precipitation patterns. *Monthly Weather Review, 145*(9), 3625–3646. https://doi.org/10.1175/MWR-D-16-0362.1

Tao, B., & Orchard, M. T. (2000). Wavelet-domain edge modeling. https://doi.org/10.1117/12.382987

Trenberth, K. E. (2011). Changes in precipitation with climate change. *Climate Research, 47*(1–2), 123–138. https://doi.org/10.3354/cr00953

Vasić, S., Lin, C. A., Zawadzki, I., Bousquet, O., & Chaumont, D. (2007). Evaluation of precipitation from numerical weather prediction models and satellites. *Monthly Weather Review, 135*(11), 3750–3766. https://doi.org/10.1175/2007MWR1955.1

Wang, R., Su, L., Wong, W. K., Lau, A. K., & Fung, J. C. (2023). Skillful radar-based heavy rainfall nowcasting using task-segmented GAN. *IEEE Transactions on Geoscience and Remote Sensing, 61*. https://doi.org/10.1109/TGRS.2023.3295211

Wang, Z., & Simoncelli, E. P. (2003). Local phase coherence and the perception of blur. *Advances in Neural Information Processing Systems*.

Wei, K., Ouyang, C., Duan, H., Li, Y., Chen, M., Ma, J., ... & Zhou, S. (2020). Reflections on the catastrophic 2020 Yangtze River Basin flooding. *The Innovation, 1*(2). https://doi.org/10.1016/j.xinn.2020.100038

Wirsing, K. (2020). Time frequency analysis of wavelet and Fourier transform. https://doi.org/10.5772/intechopen.94521

Xing, Z., Cai, M., & Li, J. (2022). Improved shallow-UWNet for underwater image enhancement. https://doi.org/10.1109/ICUS55513.2022.9986534

Yang, J., & Guan, Y. (2026). Fourier analysis of spatial point processes. *Bernoulli, 32*(1), 370–392. https://doi.org/10.3150/25-BEJ1862

Yano, J. I., Ziemiański, M. Z., Cullen, M., Termonia, P., Onvlee, J., Bengtsson, L., ... & Wyszogrodzki, A. A. (2018). Scientific challenges of convective-scale numerical weather prediction. *Bulletin of the American Meteorological Society, 99*(4), 699–710. https://doi.org/10.1175/BAMS-D-17-0125.1

Yen, M. H., Liu, D. W., Hsin, Y. C., Lin, C. E., & Chen, C. C. (2019). Application of deep learning for rainfall prediction in Southern Taiwan. *Scientific Reports, 9*(1), 12774. https://doi.org/10.1038/s41598-019-49242-6

Yibo, Z., Chengcheng, W., Pengcheng, W., Lu, Z., Qingbo, Y., Hui, X., & Maofa, W. (2023). Improving precipitation forecasting in Jilin Province using deep learning and Gaussian noise. https://doi.org/10.20944/preprints202309.0156.v1

Zhang, H., Sun, M., Yao, X., Wang, Z., & Zhang, L. (2021). Spatial–temporal distribution of tropospheric specific humidity in the arid region of northwest China. *Atmosphere, 12*(3), 349. https://doi.org/10.3390/atmos12030349

Zhang, R., Isola, P., Efros, A. A., Shechtman, E., & Wang, O. (2018). The unreasonable effectiveness of deep features as a perceptual metric. https://doi.org/10.48550/arXiv.1801.03924

Zhao, Z., Dong, X., Wang, Y., Wang, J., Chen, Y., & Hu, C. (2024). MDTNet: Multiscale deformable transformer network with Fourier space losses. *IEEE Transactions on Geoscience and Remote Sensing, 62*. https://doi.org/10.1109/TGRS.2024.3414934

Zhou, Z., Siddiquee, M. M. R., Tajbakhsh, N., & Liang, J. (2019). UNet++: Redesigning skip connections to exploit multiscale features in image segmentation. *IEEE Transactions on Medical Imaging, 39*(6), 1856–1867. https://doi.org/10.1109/TMI.2019.2959609

Zoccatelli, D., Borga, M., Viglione, A., Chirico, G. B., & Blöschl, G. (2011). Spatial moments of catchment rainfall. *Hydrology and Earth System Sciences, 15*(12), 3767–3783. https://doi.org/10.5194/hess-15-3767-2011

Supplementary Files

This is a list of supplementary files associated with this preprint. Click to download.

- Supplementaryinformation.docx